Eur. Phys. J. Appl. Phys. (2015) 70: 31101
DOI: 10.1051/epjap/2015150049

THE EUROPEAN PHYSICAL JOURNAL APPLIED PHYSICS

Regular Article

Numerical dynamo action in cylindrical containers*

Caroline Nore[1,a], Daniel Castanon Quiroz[2], Jean-Luc Guermond[1,2], Jacques Léorat[3], and Francky Luddens[1]

[1] Laboratoire d'Informatique pour la Mécanique et les Sciences de l'Ingénieur, CNRS UPR 3251, rue John von Neumann, 91403 Orsay Cedex, France
[2] Department of Mathematics, Texas A&M University 3368 TAMU, College Station, 77843-3368 TX, USA
[3] Luth, CNRS (UMR8102) and Observatoire de Paris-Meudon, Place Janssen, 92195 Meudon, France

Received: 28 January 2015 / Received in final form: 14 April 2015 / Accepted: 20 May 2015
Published online: 24 June 2015 –

Abstract. The purpose of this paper is to present results from numerical simulations of dynamo action in relation with two magnetohydrodynamics (MHD) experiments using liquid sodium in cylindrical containers. The first one is the von Kármán sodium (VKS) experiment from Cadarache (France), the second one is a precession-driven dynamo experiment from the DREsden sodium facility for DYNamo and thermohydraulic studies (DRESDYN).

1 Introduction

Still a 100 years or so after Larmor suggested that dynamo action can be at the origin of magnetic fields generated in planets and stars, the exact mechanism by which a fluid dynamo can be put in action in astrophysical bodies largely remains an open question. Experimentation in this domain is hard, and it is only recently that fluid dynamos have been produced experimentally: in 1999 for the Riga [1] and the Karlsruhe [2] experiments, and in 2006 for the VKS experiment [3]. These experiments have been very useful to validate theoretical and numerical models. For instance, in the Riga and the Karlsruhe experiments, the observed thresholds for dynamo action agreed with calculations performed with simplified velocity fields and geometries, and the observed magnetic field had the expected spatial distribution. But in the von Kármán sodium (VKS) dynamo experiment of Cadarache, the magnetic field that was observed showed a strong axisymmetric component that could not be predicted using simplified axisymmetric velocity fields and geometries. Moreover, dynamo action could be observed only when at least one of the rotating impellers driving the flow was made of soft iron. It is now recognized, although not fully understood, that the high magnetic permeability of the impellers plays a crucial role in the selection of the axisymmetric mode in the VKS dynamo experiment [4]. The quest for experimental dynamo action is currently pursued in Europe through an ambitious project at the DREsden sodium facility for DYNamo and thermohydraulic studies (DRESDYN) [5]. Among the objectives of this project is the study of the action of precession as a large scale driving force, which some think may be more compatible with natural dynamos [6]. This will be done in a precession-driven dynamo experiment composed of a cylinder of aspect ratio one: the diameter and the height of the cylinder are equal to 2 m. The cylinder will be filled with liquid sodium and will undergo rotation about its axis and precession about another axis (which can be the equator). The planned maximum rotation and precession frequencies are 10 Hz and 1 Hz, respectively.

Even though numerical simulations of the VKS and DREsden experiments with realistic kinetic Reynolds numbers are out of reach with present day computers, we think that numerical simulations are useful complements and can shed some light on specific aspects of these experiments. The main motivation of the present paper is to present an overview of the studies that we have done over the years to better understand dynamo action in cylindrical vessels like those used in the VKS and the DREsden experiments. We have developed for this purpose a nonlinear magnetohydrodynamics (MHD) code called SFEMaNS (for spectral/finite elements for the Maxwell and Navier-Stokes equations). This code solves the nonlinear incompressible MHD equations in heterogeneous cylindrical domains. The spatial approximation is done with Fourier expansions in the azimuthal direction and Lagrange finite elements in the meridional section (see Refs. [7–9] for more details). The spatial distribution of the electrical conductivity and the magnetic permeability is allowed to be discontinuous in the meridian section and highly heterogeneous (but continuous) in the azimuthal direction; the magnetic domains can be composed of conducting and non-conducting parts. The code

[a] e-mail: caroline.nore@limsi.fr

* Contribution to the topical issue "Electrical Engineering Symposium (SGE 2014) – Elected submissions", edited by Adel Razek

has been thoroughly validated on numerous manufactured solutions and against other MHD codes on linear [10–12] and nonlinear magnetohydrodynamics problems [8].

The paper is organized as follows. Section 2 presents results related to the VKS experiment: Section 2.2 summarizes results obtained with a kinematic model involving an axisymmetric flow that generates only non-axisymmetric magnetic fields [9]; Section 2.3 presents new results obtained with a mean-field model that produces an axisymmetric magnetic field very similar to that obtained experimentally (see also Ref. [13]). Section 2.4 investigates the von Kármán experimental set-up with an accurate representation of the curved blades and their ferromagnetic permeability. The three kinematic studies of Section 2 underline the crucial role played by the soft iron impellers in the VKS dynamo and corroborate the conclusions from reference [4]. A speculative mechanism for dynamo action in the VKS experiment is proposed in Section 2.5. Section 3 presents studies in relation with the precession-driven experiment at the DRESDYN facility. It is numerically demonstrated in this section that, if strong enough, precession can generate dynamo action in a rotating cylinder filled with a conducting fluid [14]. It is also shown that using lateral walls made of copper helps the dynamo effect.

2 Kinematic dynamo action in a VKS-like configuration

2.1 Motivation

We want to analyze the effect of ferromagnetic material on dynamo action by using various kinematic dynamo models in configurations similar to the von Kármán sodium experiment. In Section 2.2, we use the axisymmetric velocity field measured by the CEA Saclay team [15] in a mock-up of the experimental set-up using water; the field is averaged in time and in azimuth. The geometry of the container and the electrical conductivity and magnetic permeability of its various parts are modeled realistically, but the geometry of the blades is simplified in the azimuthal direction, i.e., the blades are only accounted for in average. In Section 2.3, we use a simpler analytical velocity field (MND), which is a good approximation of the measured velocity field [16], and use a simpler axisymmetric geometry to focus our efforts on a more physically relevant modeling of the small scales of the velocity field and of the interactions with the blades of the impellers. In Section 2.4, we model half of the von Kármán experimental set-up with half of the MND flow but with the real geometry of the impellers, i.e., the curved blades with their ferromagnetic permeability are accurately represented.

2.2 Equatorial dipole

The first kinematic dynamo problem that we investigate solves the following equations written in non-dimensional units:

$$\partial_t \mathbf{B} = \boldsymbol{\nabla} \times (\mathbf{u} \times \mathbf{B}) - \frac{1}{R_\mathrm{m}} \boldsymbol{\nabla} \times \left(\frac{1}{\sigma_r} \boldsymbol{\nabla} \times \left(\frac{\mathbf{B}}{\mu_r} \right) \right), \quad (1)$$

$$\boldsymbol{\nabla} \cdot \mathbf{B} = 0, \quad (2)$$

where $\mathbf{B}$ is the induction field, and σ_r, μ_r are the relative conductivity and permeability of the various materials in presence. The parameters σ_r, μ_r are not constant since the walls and the impellers may be composed of copper, steel or soft iron. Denoting by U the characteristic velocity scale, σ_0 the electrical conductivity of the liquid sodium, ρ its density, μ_0 the magnetic permeability of vacuum, the magnetic induction is made non-dimensional by using $B = U\sqrt{\rho\mu_0}$. The quantity $R_\mathrm{m} = \mu_0\sigma_0 U R_0$ is the magnetic Reynolds number, where R_0 is the characteristic length scale. In the following, we use cylindrical coordinates r, θ, z and refer to individual azimuthal Fourier modes $e^{im\theta}$ by the integer m.

2.2.1 Numerical settings for the standard kinematic model

The left panel of Figure 1 shows a sketch of the VKS experiment; the simplified geometry that is used in the numerical simulations is shown in the right panel. The conducting domain is partitioned into a moving region (comprising the "bulk", "lid" and the "disk" flows) and a static region (comprising the side layer and the copper vessel). We choose the reference length scale, R_0, to be the radius of the inner vessel. The liquid sodium in the region $(r, z) \in [0, R_0]\times[-1.275R_0, 1.275R_0]$ is allowed to move, but the liquid sodium in the so-called "side layer", $r \in [R_0, 1.4R_0]$, is stagnant. The region where the fluid is allowed to move is further divided into the "bulk flow" subregion $(r, z) \in [0, R_0]\times[-0.9R_0, 0.9R_0]$, the "disk flows" subregions $(r, z) \in [0, R_0]\times[-0.975R_0, -0.9R_0]\cup[0.9R_0, 0.975R_0]$ and the "lid flows" subregions $(r, z) \in [0, R_0]\times([-1.275R_0, -0.975R_0] \cup [0.975R_0, 1.275R_0])$. The purpose of the"disk flows" is to model the two impellers and the fluid moving between the blades. We also introduce two "flat disks" of thickness $H_i = 0.075R_0$ and radius $R_i = 0.75R_0$ to account for the presence of solids of various material properties in the "disk flows" subregions; these two disks are modeled with round edges at the periphery. The geometry of the external copper wall of the device is defined by $(r, z) \in [1.4R_0, 1.6R_0]\times[-1.475R_0, 1.475R_0]$.

The conductivity of the moving fluid, σ_0, and that of the stagnant fluid, σ_1, are set to be equal to that of liquid sodium σ_0. The outer wall of the device has the conductivity of copper, $\sigma_2 = 4.5\sigma_0$. The magnetic permeability of every component of the device is equal to that of vacuum, μ_0, except for the two "flat disks". Two different material compositions are tested for the "flat disks". In what we hereafter refer to as case A and case B, the "flat disks" are made of stainless steel, $\sigma_i = 0.14\sigma_0$ and $\mu_i = \mu_0$, but in case C and case D the "flat disks" are made of soft iron, $\sigma_i = \sigma_0$ and $\mu_i = 60\mu_0$ [17].

The prescribed axisymmetric velocity field $\mathbf{u}$ is defined separately in the "bulk flow", "disk flows" and "lid flows"

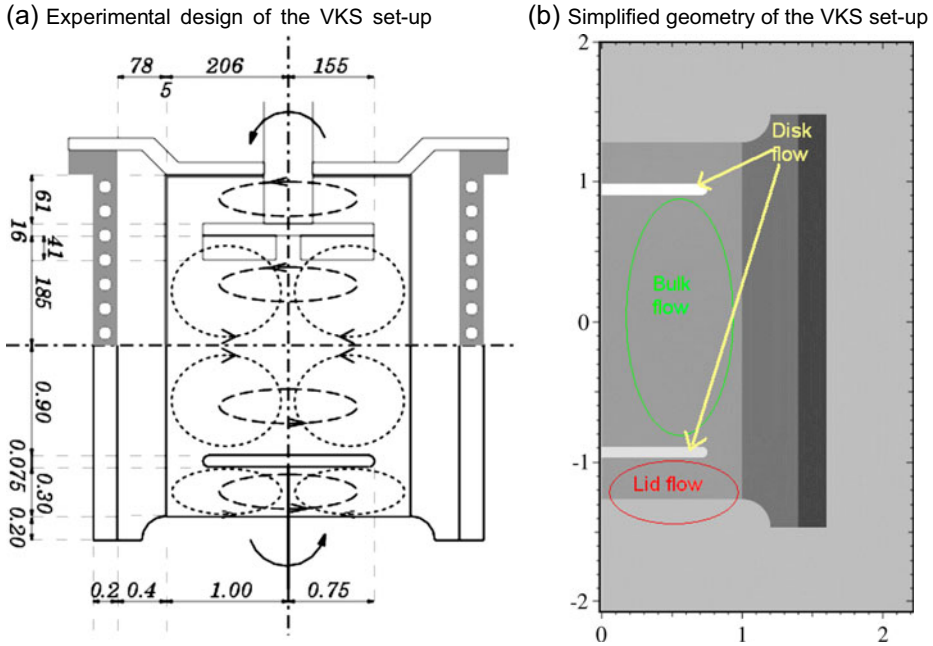

Fig. 1. Von Kármán sodium (VKS) experiment: (a) experimental configuration and structure of the averaged velocity field: (top) real dimensions (courtesy of the VKS-CEA Saclay team); (bottom) simplified geometry used in this section; (b) geometry used in SFEMaNS with the "Bulk", "Lid" and "Disk" flows.

regions. In the "bulk flow" region, $\mathbf{u}$ is modeled by using the axisymmetric time-averaged flow field measured in a water experiment documented in reference [15]. The reference scale U is defined to be the maximum of the Euclidean norm of the experimental velocity field. Let us denote by $u_0(r,z)\mathbf{e}_\theta$ the axisymmetric "bulk flow". Then the flow in the top "disk flow" region is defined to be equal to $u_0(r,0.9)\mathbf{e}_\theta$ and the flow in the bottom "disk flow" region is defined to be equal to $u_0(r,-0.9)\mathbf{e}_\theta$. Finally, two different models are tested for the "lid flows". In the first model, the velocity field of the top "lid flow" is defined to be the linear interpolation with respect to z between $u_0(r,0.9)\mathbf{e}_\theta$ and zero; the bottom flow is defined similarly. The "lid flow" is henceforth denoted $\mathbf{u}_\theta^{\rm lin}$. In the second model the "lid flow" velocity is defined to be the sum of $\mathbf{u}_\theta^{\rm lin}$ and 10% of an analytical poloidal recirculation flow $\mathbf{u}^{\rm pol}$ that has been introduced in reference [16]. The flow $\mathbf{u}^{\rm pol}$ is normalized so that the maximum of Euclidean norm of $\mathbf{u}^{\rm pol}$ is also U. The exact nature of the lid flows for the cases A, B, C and D is reported in Table 1.

2.2.2 Numerical results for the mode m = 1

As a consequence of Cowling's theorem [18], it is known that an axisymmetric velocity field cannot give rise to an axisymmetric magnetic field in an axisymmetric configuration (geometry and material properties). Therefore only non-axisymmetric Fourier modes can be linearly unstable. We evaluate the growth rate of the magnetic energy for the four cases defined above by solving equation (1) for various Reynolds numbers. The critical magnetic Reynolds number $R_{\rm m}^c$ corresponds to zero growth rate. The results are reported in the rightmost column of Table 1. It turns out that in our numerical simulations, it is always the mode $m = 1$ that is the most unstable. When the two disks are made of stainless steel, the two different lid flows lead to different thresholds ($R_{\rm m}^c = 82$ and $R_{\rm m}^c = 75$, respectively). Using ferromagnetic disks decreases significantly the threshold to either $R_{\rm m}^c = 64$ or 66 and makes it insensitive to the lid flows. The beneficial effect of using ferromagnetic material was also observed in computations reported in reference [9], where we imposed the Dirichlet condition $\mathbf{H}\times\mathbf{n} = 0$ on the disks (corresponding to perfect ferromagnetic disks) and used a simplified geometry of the container discarding the region $|z| > 0.7$. In this case we obtained $R_{\rm m}^c(m = 1) = 40$. The detrimental effect of the lid flows has also been observed in reference [19].

Table 1. Critical magnetic Reynolds number for the Fourier mode $m = 1$ in VKS simplified setting.

Case	Disk composition	Lid flow	$R_{\rm m}^c$
A	Stainless steel	$\mathbf{u}_\theta^{\rm lin}$	82
B	Stainless steel	$\mathbf{u}_\theta^{\rm lin} + 10^{-1}\times\mathbf{u}^{\rm pol}$	75
C	Soft iron	$\mathbf{u}_\theta^{\rm lin}$	66
D	Soft iron	$\mathbf{u}_\theta^{\rm lin} + 10^{-1}\times\mathbf{u}^{\rm pol}$	64

We show in Figure 2 the two unstable modes of the magnetic field corresponding to cases B and D. They look similar in the "bulk flow" region. They are characterized by an equatorial dipole and two vertical structures of opposite sign near the axis. Noticeable differences are apparent when observing the magnetic lines close to the counter-rotating disks.

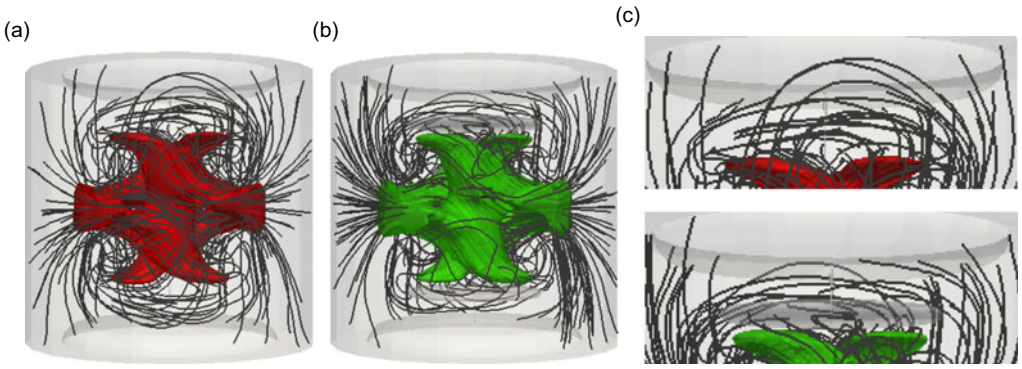

Fig. 2. Magnetic field lines and isovalues of the magnetic energy (25% of the maximum magnetic energy) for cases B and D. From reference [9]. Note the magnetic lines focusing in the disk in the bottom figure in panel (c). (a) $\mu = 1$; $R_\mathrm{m} = 75$, (b) $\mu = 60$; $R_\mathrm{m} = 65$, (c) view of top containers.

The conclusion of this series of computations is that ferromagnetic disks have a measurable impact on the dynamo threshold, which is crucial since the experimental magnetic Reynolds number is constrained to be below 50 by the power available in the VKS2 experiment. Another noticeable effect of ferromagnetic disks is that they shield the "bulk flow" from the influence of the "lid flows".

2.3 Axial dipole

As stated above, in order to get a growing axisymmetric magnetic field, we need to model the non-axisymmetric scales of the velocity field realized in the VKS experiment which we neglected in the above section. We have chosen to use the so-called *mean-field* dynamo theory from reference [20] to account for the effects of these velocity perturbations. Denoting by $\mathbf{u}'$ the small scale flow and by $\mathbf{b}'$ the induced small scale magnetic induction, the mean field approach consists of assuming that the mean electromotive force induced by the small scales of the velocity field is a linear function of the mean magnetic induction $\mathbf{B}$ and its first derivative:

$$\langle \mathbf{u}' \times \mathbf{b}' \rangle_i = \mathbb{a}_{ij} B_j + \beta_{ijk} \partial_j B_k. \tag{3}$$

The tensors $\mathbb{a}_{ij}$ and β_{ijk} are a priori anisotropic since the flow between the blades is strongly anisotropic. In the following, we neglect the contribution from β assuming that the dominant effects result from the α-effect described by the trace of $\mathbb{a}_{ij}$. Heuristic arguments suggest [21,22] that the dominant coefficients of the tensor $\mathbb{a}$ are $\mathbb{a}_{zz}$ and $\mathbb{a}_{\theta\theta}$ and these coefficients should be non-positive. In the rest of this section, we set $\mathbb{a}_{zz} = 0$ and only keep $\mathbb{a}_{\theta\theta}$ since previous studies [10] have shown that the action of $\mathbb{a}_{\theta\theta}$ is enough to close the dynamo loop. We further assume that the action of the α-effect is confined to the blade region only. This assumption is formalized by setting $\mathbb{a}_{\theta\theta} = \alpha\chi$, where χ is equal to 1 in the cylindrical volume swept by the blades ($0.7 \leq |z| \leq 0.9$; $r \leq 0.9$) and χ is equal to zero outside the blade domain. Details can be found in reference [13].

The non-dimensional mean field equation is written as follows:

$$\partial_t \mathbf{B} = \boldsymbol{\nabla} \times \left((\mathbf{u} \times \mathbf{B}) + \alpha\chi (\mathbf{B} \cdot \mathbf{e}_\theta) \mathbf{e}_\theta \right) - \frac{1}{R_\mathrm{m}} \boldsymbol{\nabla} \times \left(\frac{1}{\sigma_r} \boldsymbol{\nabla} \times \left(\frac{\mathbf{B}}{\mu_r} \right) \right), \tag{4}$$

where σ_r and μ_r are the relative electrical conductivity and magnetic permeability fields, respectively. In this section we assume that the conductivity is constant everywhere ($\sigma_r = 1$), since we have shown in reference [11] that the key material property for magnetic storage in the impellers is the magnetic permeability. The relative permeability in the disks is chosen to be $\mu_d = 60$, which is a value close to that measured in reference [17] for the soft iron impellers used in the VKS experiment.

To avoid the increase of resolution that would be required to simulate correctly the magnetic boundary conditions on the blades, we finally use another simplifying hypothesis by modeling the eight soft iron blades of the real impellers in the domain swept by the blades ($0.7 \leq |z| \leq 0.9, r \leq 0.9$) with an axisymmetric distribution of effective relative magnetic permeability in the range $1 < \mu_b < \mu_d$.

2.3.1 Numerical settings for the α-model

We model the VKS device as a vessel composed of two concentric cylindrical containers closed at their extremities by two thin lids. (The exact configuration of the VKS experiment is described in the previous Fig. 1a.) The radius of the inner cylinder is henceforth defined to be the length unit, say R_0. The non-dimensional radius of the external cylinder is $R_\mathrm{e} = 1.4$ and the non-dimensional height of the vessel is $L = 2.6$. The computational domain, $0 \leq r \leq R_\mathrm{e}$, $0 \leq \theta \leq 2\pi$, $|z| \leq L/2$, is denoted $\mathcal{D}$, see Figure 3.

The vessel is assumed to be filled with liquid sodium, and the sodium enclosed between the inner and outer cylinders is kept stagnant at all times. The two impellers mounted at the extremities of the inner cylinder are each

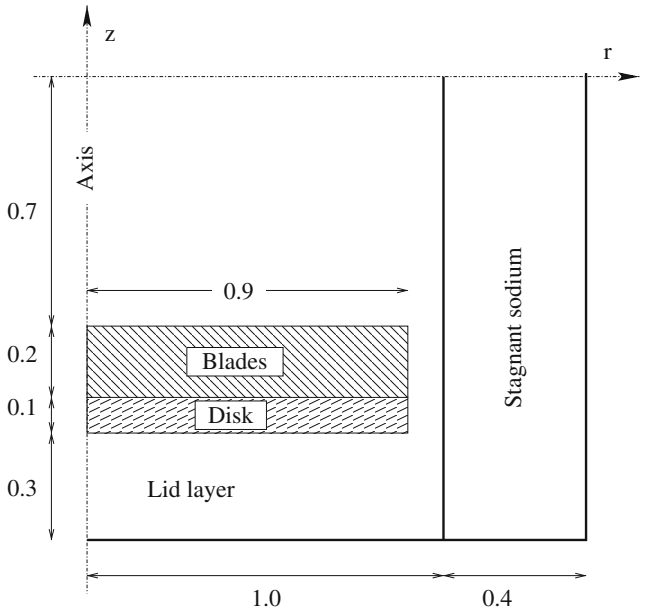

Fig. 3. Bottom half of the meridian section of the VKS numerical model for the α-model.

composed of a disk equipped with eight blades. The thickness and radial extension of the disks is 0.1 and 0.9, respectively, i.e., the region occupied by the disks is $0 \leq r \leq 0.9$, $0 \leq \theta < 2\pi$, $0.9 \leq |z| \leq 1$, see the shaded region labeled "Disk" in Figure 3. The relative magnetic permeability of the disks is denoted μ_d. When rotating, the eight blades sweep a volume of height 0.2 and radius 0.9, i.e., the region occupied on average by the blades is $0 \leq r \leq 0.9$, $0 \leq \theta < 2\pi$, $0.7 \leq |z| \leq 0.9$, see the region with diagonal pattern labeled "Blades" in Figure 3. The magnetic action of the blades is modeled by assigning an axisymmetric distribution of effective relative magnetic permeability to this volume, μ_b. The fluid enclosed between the two blade regions is free to move about in the inner cylinder. The vertical extension of this column of liquid sodium is denoted $2h$. We fix $h = 0.7$ in the following.

The non-dimensional velocity field in the region $0 \leq r \leq 1$, $0 \leq \theta < 2\pi$, $|z| \leq h$ is modeled by an analytical approximation of the averaged flow measured in a water model [16]:

see equation (5) at the bottom of this page.

This vector field is henceforth called the MND flow in reference to the authors (Marié-Normand-Daviaud) of reference [16]. The parameter ϵ measures the ratio between the toroidal and poloidal components of the velocity field. We choose $\epsilon = 0.7259$ in the rest of the paper since this ratio has been shown in reference [15], Figs. 9 and 10 to minimize the dynamo threshold. Note that the maximum of the Euclidean norm of the field (5) is equal to 1, (this means that the reference velocity scale U is equal to the maximum of the MND flow). With $h = 0.7$ the volume swept by the blades is not included in the MND flow. The velocity in the volume $0 \leq r \leq 1$, $0 \leq \theta < 2\pi$, $h \leq |z| \leq 1$, which is the blade and disk region, is assumed to be purely azimuthal and equal to the azimuthal component of the flow at $z = \pm h$, i.e., upon defining $\mathrm{sgn}(z) = z/|z|$, we set:

$$\begin{aligned} u_r(r,z) &= 0, \\ u_\theta(r,z) &= -4\,\mathrm{sgn}(z)\epsilon r(1-r), \\ u_z(r,z) &= 0. \end{aligned} \qquad \begin{cases} 0 \leq r \leq 1, \\ 0 \leq \theta < 2\pi, \\ h \leq |z| \leq 1. \end{cases} \quad (6)$$

A lid-layer flow is also assumed to be established behind each impeller (i.e., in the domain $0 \leq r \leq 1$, $0 \leq \theta < 2\pi$, $1 \leq |z| \leq L/2$, see "Lid layer" in Fig. 3) and the corresponding velocity field is modeled by setting:

see equation (7) at the bottom of this page.

The MND flow (5) is a reasonable divergence-free approximation of the mean axisymmetric velocity field measured in water experiments using the same driving mechanisms as in the VKS experiment [15,16].

2.3.2 Numerical results for the m = 0 mode

In the rest of this section we use $R_\mathrm{m} = 30$, $\mu_b = 10$, and for the permeability of the disks we set $\mu_d = 60$.

Figure 4a shows the largest growth rate of the axisymmetric modes with dipolar symmetry (solid line curve) and with quadrupolar symmetry (dotted-line curve) for $\alpha \in [-0.03, 0.05]$. Dynamo action occurs for $\alpha \leq \alpha_c \approx -0.025$ (for the $m = 0$ dipolar mode) and no dynamo is obtained for positive values of α. The bifurcation happening at α_c is of Hopf type; for instance, for $\alpha = -0.03$, the growth rate of the dipolar mode is $\sim$0.014 and the oscillation period is $T = 2\pi/f = 2\pi/0.072 \approx 87$. We consider

$$\begin{aligned} u_r(r,z) &= -(\pi/2h)r(1-r)^2(1+2r)\cos(\pi z/h)\,, \\ u_\theta(r,z) &= -4\epsilon r(1-r)\sin(\pi z/2h), \\ u_z(r,z) &= (1-r)(1+r-5r^2)\sin(\pi z/h). \end{aligned} \qquad \begin{cases} 0 \leq r \leq 1, \\ 0 \leq \theta < 2\pi, \\ |z| \leq h. \end{cases} \quad (5)$$

$$\begin{aligned} u_r(r,z) &= 0, \\ u_\theta(r,z) &= -4\,\mathrm{sgn}(z)\epsilon r(1-r)(L-2|z|)/(L-2), \\ u_z(r,z) &= 0. \end{aligned} \qquad \begin{cases} 0 \leq r \leq 1, \\ 0 \leq \theta < 2\pi, \\ 1 \leq |z| \leq L/2. \end{cases} \quad (7)$$

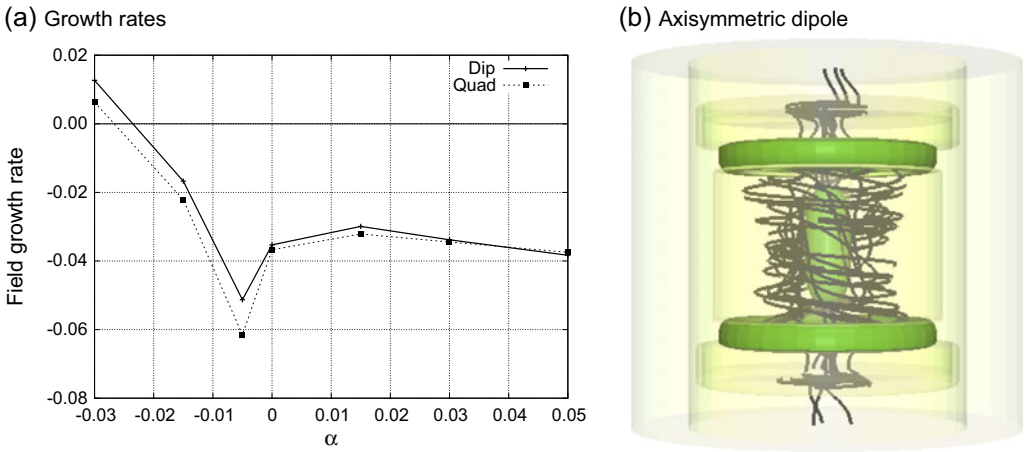

Fig. 4. (a) Largest growth rates of axisymmetric modes for $\alpha \in [-0.03, 0.05]$, $R_\mathrm{m} = 30$, $\mu_b = 10$ and $\mu_d = 60$ (dipolar and quadrupolar eigenvectors), (b) dipolar $m = 0$ mode with $\mu_d = 60$, $\mu_b = 10$, $R_\mathrm{m} = 30$ and $\alpha = -0.03$: isosurface of 20% of the maximum of the magnetic energy and magnetic field lines (in black).

that the value of the threshold, $\alpha_c \approx -0.025$, is realistic since the maximal speed of the MND velocity field is 1 in our advective units, (recall that α scales like a velocity).

The spatial structure of the $m = 0$ dipolar mode is shown in Figure 4b: are plotted the isosurface of 20% of the maximum of the magnetic energy and the magnetic field lines (in black). This structure is very similar to the magnetic field measured at saturation in the VKS experiment (see Fig. 6b in Ref. [23]).

2.3.3 Similarities with the VKS dynamo

In conclusion, the kinematic dynamo simulations presented in this section are based on a mean-field model relying on three phenomenological parameters: the magnetic permeability of the disks, μ_d; the effective permeability of the domain swept by the blades, μ_b; the component $\mathrm{a}_{\theta\theta}$ of the α-tensor. For the α-effect model to be effective with realistic values of α, i.e., a few percents of the reference velocity scale, it is necessary to have a large value of μ_d. For the critical magnetic Reynolds number to be within the limits of the power supply available in the VKS experiment, it is also necessary that the blades be made of a material of moderately large permeability.

The model exhibits features that are all observed in the VKS experiment:

- dynamo action occurs at $R_\mathrm{m} = 30$ using a realistic value of α (say $\alpha = -0.03$) when the disks are composed of soft iron and the effective permeability in the region swept by the blades is large enough ($\mu_b = 10$),
- the two most unstable modes at $R_\mathrm{m} = 30$ are axisymmetric and have dipolar and quadrupolar symmetry, respectively. The most unstable mode is the axisymmetric dipole. This mode is dominated by the B_z component close to the axis and by the B_θ component in the vicinity of the impellers (see Fig. 4b). The spatial distribution of this mode is very close to that observed at saturation in the VKS experiment (see Fig. 6b of Ref. [23]).

2.4 Non axisymmetric dynamo action with ferromagnetic blades

We now model half of the von Kármán experimental setup [23], which is schematically represented on Figure 1a. This time the blades are realistically represented. We solve again the non-dimensional induction field equation (1) with a kinematic velocity field:

$$\partial_t \mathbf{B} = \boldsymbol{\nabla} \times (\mathbf{u} \times \mathbf{B}) - \frac{1}{R_\mathrm{m}} \boldsymbol{\nabla} \times \left(\frac{1}{\sigma_r} \boldsymbol{\nabla} \times \left(\frac{\mathbf{B}}{\mu_r} \right) \right). \quad (8)$$

In this section, we assume that the conductivity is constant everywhere ($\sigma_r = 1$).

2.4.1 Numerical settings for the half MND model

The computational domain is a cylindrical vessel of radius $R_c = 1$ and height $h = 0.7$ ($0 \le r \le 1$, $-0.2 \le z \le 0.5$). The impeller driving the flow consists of a disk equipped with eight blades. The disk is a cylinder of radius $R_d = 0.54$ and height $l_d = 0.06$ ($-0.2 \le z \le -0.14$). The height of the blades is $l_b = 0.14$, their thickness is $e_b = 0.02$, the angle at the rim is $\alpha = 24°$ and the generator radius is $R_g = 0.66$ (see Fig. 5a). This geometry is shown in Figure 5b.

The velocity field, $\mathbf{V}_F = (u_r, u_\theta^F, u_z)$, in the fluid ($0 \le r \le 1$, $0 \le z \le 0.5$) is modeled as follows:

$$\begin{aligned} u_r &= (\pi/2L)\cos(\pi z/L)\, r(1-r)^2(1+2r), \\ u_\theta^F &= 4\epsilon r(1-r^5)\sin(\pi(L-z)/2L), \\ u_z &= -(1-r)(1+r-5r^2)\sin(\pi z/L), \end{aligned} \quad (9)$$

where $L = 0.5$ denotes the distance between the top lid of the computational box (i.e., equatorial plane of the VKS container) and the top of the blades, and ϵ measures the ratio between the toroidal and the poloidal components of the velocity (here, $\epsilon = 0.7259$ as in Ref. [16]). The velocity

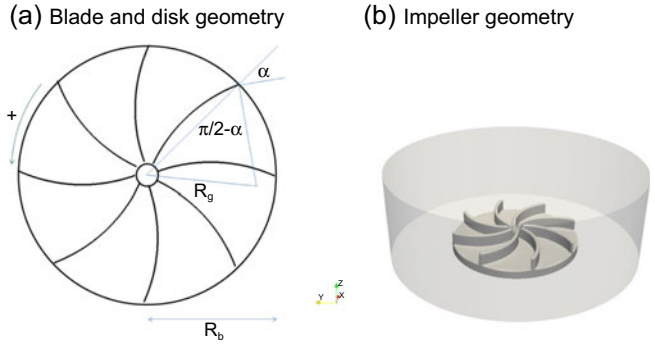

Fig. 5. (a) Geometric parameters defining the blades; (b) impeller mesh used in SFEMaNS for the half von Kármán set-up.

field in the impeller region ($0 \leq r \leq 1$, $-0.2 \leq z \leq 0$) is assumed to be a solid-body rotation:

$$u_\theta^I = r. \tag{10}$$

The component u_θ is interpolated between the fluid region and the impeller zone using $u_\theta = u_\theta^F \frac{1+\tanh(z/z_{\rm del})}{2} + u_\theta^I \frac{1-\tanh(z/z_{\rm del})}{2}$, with $z_{\rm del} = 0.05$. The vector field defined above is denoted $\mathbf{V}_0$ and its maximum Euclidean norm is $U_{\max} = 1.66$. All the computations presented in this section are performed in the reference frame of the impeller, i.e., the velocity field in equation (8) is defined to be $\mathbf{u} := \mathbf{V}_0 - r\mathbf{e}_\theta$.

The boundary conditions are defined as follows: $(\mathbf{B}/\mu_r)\times\mathbf{n} = \mathbf{0}$, corresponding to an infinite permeability boundary on the side of the vessel (at $r = 1$, $-0.2 \leq z \leq 0.5$) and on the top lid ($z = 0.5$, $0 \leq r \leq 1$) and bottom lid ($z = -0.2$, $0 \leq r \leq 1$).

2.4.2 Numerical results for the non-axisymmetric dynamo action

Due to the dependence of the magnetic permeability with respect to the azimuth angle, the eigenvalue problem associated with equation (8) has five disconnected families of eigenspaces. More specifically, since the magnetic permeability is supported by the Fourier modes $e^{8ik\theta}$, $k \in \mathbb{Z}$, the term $\boldsymbol{\nabla} \times \left(\frac{1}{\sigma_r}\boldsymbol{\nabla} \times \left(\frac{\mathbf{B}}{\mu_r}\right)\right)$ couples the modes in the following vector spaces: span$\{e^{8ik\theta}, k \in \mathbb{Z}\}$, span$\{e^{i(\pm 1+8k)\theta}, k \in \mathbb{Z}\}$, span$\{e^{i(\pm 2+8k)\theta}, k \in \mathbb{Z}\}$, span$\{e^{i(\pm 3+8k)\theta}, k \in \mathbb{Z}\}$ and span$\{e^{i(4+8k)\theta}, k \in \mathbb{Z}\}$. We henceforth refer to the above five vector spaces as the 0-family, the 1-family, etc. Given any initial data for equation (8) with nonzero projection on the five families, long time integration of the equation gives a magnetic field which is a superposition of the leading eigenvectors in each family. The corresponding eigenvectors are obtained by projecting the magnetic field on each of the above families.

Setting $\mu_b = \mu_d = 5$, we measure the leading eigenvalues of each family for the magnetic Reynolds numbers $R_{\rm m} = 90$, $R_{\rm m} = 550$ and $R_{\rm m} = 750$ (data not shown). The simulations at $R_{\rm m} = 750$ show that the leading mode of the 0-family has a negative growth-rate; the spatial distribution of the corresponding eigenvector is shown in Figure 6a. This field is mainly azimuthal and axisymmetric in the disk (which can be considered as a reservoir of toroidal field), it is concentrated in the blades (where it is poloidal and non-axisymmetric with a $m = 8$ structure), and it is mainly vertical and axisymmetric in the bulk. This structure is very similar to the measured magnetic field reported in reference [23]. The leading eigenvector in the 2-family at $R_{\rm m} = 750$ has a positive growth-rate; the spatial distribution of this mode is shown in Figure 6b. It is a bulk eigen-mode.

We have estimated the thresholds for the 0- and 2-families by interpolation (or extrapolation) on the growth rates at $R_{\rm m} = 90$, $R_{\rm m} = 550$ and $R_{\rm m} = 750$. The dynamo threshold is $R_{\rm m}^c \approx 1300$ for the 0-family and $R_{\rm m}^c \approx 550$ for the 2-family.

2.5 Scenario for the VKS dynamo

The computations from Sections 2.3 and 2.4 are coherent and lead us to propose a mechanism for the VKS dynamo

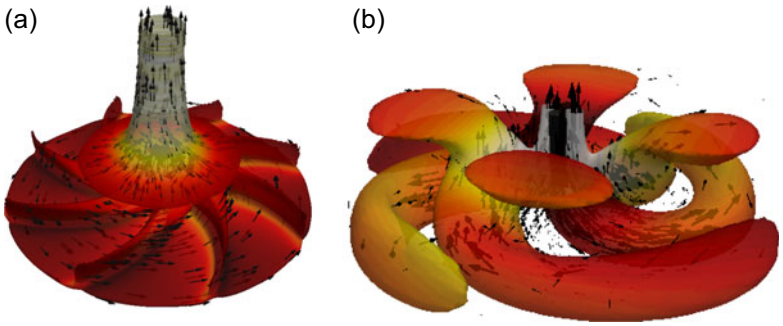

Fig. 6. (a) Structure of the leading eigenvector in the 0-family (stable) and (b) leading eigenvector in the 2-family (un-stable) represented by the isosurface $\|\mathbf{B}\|^2$ (respectively 0.5% and 10% of maximum value, colored by the vertical component with minimum value in brown and maximum value in white) and vectors shown in the disk, in the impeller region and in the bulk region. Half von Kármán set-up with the velocity field $\mathbf{V}_0$ at $R_{\rm m} = 750$ with $\mu_b = \mu_d = 5$.

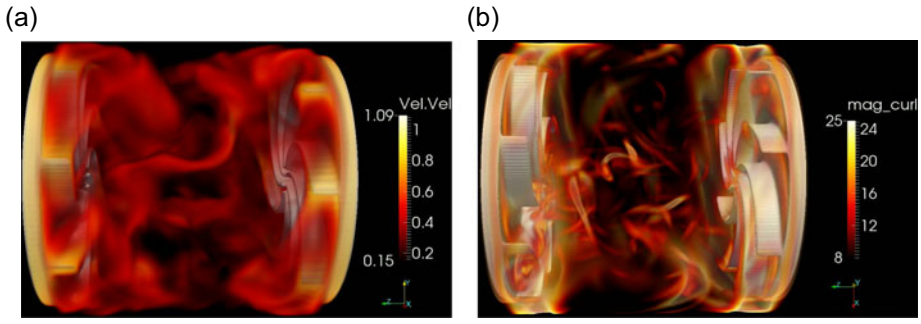

Fig. 7. Preliminary Navier-Stokes simulations in the TM73 VKS configuration at $R_e = 2400$. (a) Euclidean norm of velocity, (b) vorticity.

based on four steps:

1. the Ω-effect generates a toroidal magnetic field from poloidal magnetic field seeds,
2. the azimuthal magnetic field is stored in the high permeability disk (cf. [12]) as in Figure 6a,
3. the azimuthal field is collected in the blades and transformed into a poloidal field as in Figure 6a,
4. focusing of the poloidal components gives rise to the vertical component on the axis as in Figure 6a.

The accumulation of azimuthal energy in the disks is supported by previous studies reported in references [11,12]. It is shown therein that the disks have a strong tendency to store azimuthal energy as μ_d grows (see Figs. 5 and 6 in Ref. [12] and Figs. 5 and 7 in Ref. [11]). Moreover the linear stability analysis (without alpha modeling) shows that the axisymmetric mode (though decaying) is dominant when $\mu_d \geq 18$ (see Fig. 5 in Ref. [12]). The recirculating velocity field between the blades interacts with the axisymmetric azimuthal mean field that dominates in the neighborhood of the disks. The small scales radial perturbations of the magnetic field are focalized and amplified by the blades when μ_b is large as shown in reference [24]; this is the localized alpha effect.

This mechanism is still speculative and its validation would require a better knowledge of the fluid flow between the blades, which is a task that we are currently undertaking using a pseudo-penalty technique similar to that used in reference [25]. Some preliminary results of Navier-Stokes simulations in the VKS configuration at $R_e = 2400$ are shown in Figure 7.

3 Nonlinear dynamo action in a precessing cylinder

3.1 Motivation

The idea that precession can be a potent mechanism to drive dynamo action for the Earth has long been debated (see for example [6]). Modern astrophysical observations of some planetary dynamos can contribute to resolve this issue but definite evidence is still lacking. Because of the large computing resources required, it is only recently that numerical computations have demonstrated that dynamo action occurs in different precessing containers: spherical [26] and spheroidal [27] ones. Since neither spheres nor spheroids are convenient for large-scale experiments, it is instructive to investigate whether similar results can be obtained in cylindrical containers.

3.2 Numerical settings

Let us consider a cylindrical vessel of radius R and height L. The vessel contains a conducting fluid and is embedded in vacuum. The container rotates about its axis of symmetry with angular velocity $\Omega_r \mathbf{e}_z$ and is assumed to precess about a second axis spanned by the unit vector $\mathbf{e}_p$ forming an angle α with $\mathbf{e}_z$, $(0 < \alpha < \pi)$. The precession angular velocity is $\Omega_p \mathbf{e}_p$. We use the cylindrical coordinate system centered at the center of mass of the cylinder, say O; the Oz axis is the line passing through O and parallel to $\mathbf{e}_z$; the origin of the angular coordinate $\theta\,(0 \leq \theta < 2\pi)$ is the half plane passing through O, spanned by $\mathbf{e}_z$ and $\mathbf{e}_p$, and containing $\Omega_p \mathbf{e}_p$. The third coordinate, denoted r, is the distance to the Oz axis.

Let R and $U = R\Omega_r$ be the reference length and velocity scales, respectively. The fluid density, ρ, is assumed to be constant and the reference pressure scale is $P := \rho U^2$. The magnetic permeability is uniform throughout the entire space, μ_0, and the electric conductivity of the conducting fluid is constant, σ_0. The quantities μ_0 and σ_0 are used as reference magnetic permeability and electric conductivity, respectively. The reference scale for the magnetic field is chosen so that the reference Alfvén speed is 1, i.e., $B := U\sqrt{\mu_0 \rho}$. We are left with five non-dimensional parameters: the aspect ratio L/R, the precession angle α, the precession rate $\varepsilon = \Omega_p/\Omega_r$ and two fluid parameters, namely the kinetic Reynolds number $R_e = R^2\Omega_r/\nu$ (where ν is the kinematic viscosity) and the magnetic Reynolds number $R_m = \mu_0\sigma_0 R^2 \Omega_r$. In the following, we impose $L/R = 2$, $\varepsilon = 0.15$ and $\alpha = \pi/2$, see Figure 8.

The non-dimensional set of equations that we consider is written as follows in the precessing frame of reference:

$$\partial_t \mathbf{u} + (\mathbf{u}\cdot\nabla)\mathbf{u} + 2\varepsilon \mathbf{e}_p \times \mathbf{u} + \boldsymbol{\nabla} p = \frac{1}{R_e}\Delta \mathbf{u} + \left[\boldsymbol{\nabla} \times \left(\frac{\mathbf{B}}{\mu_r}\right)\right] \times \mathbf{B}, \quad (11)$$

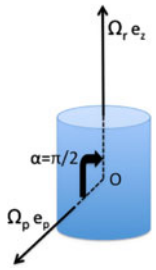

Fig. 8. Definition of the rotation and precession axes.

$$\boldsymbol{\nabla}\cdot\mathbf{u}=0, \tag{12}$$

$$\partial_t\mathbf{B}=\boldsymbol{\nabla}\times(\mathbf{u}\times\mathbf{B})-\frac{1}{R_\mathrm{m}}\boldsymbol{\nabla}\times\left(\frac{1}{\sigma_r}\boldsymbol{\nabla}\times\left(\frac{\mathbf{B}}{\mu_r}\right)\right), \tag{13}$$

$$\boldsymbol{\nabla}\cdot\mathbf{B}=0, \tag{14}$$

where $\mathbf{u}$, p and $\mathbf{B}$ are the velocity field, the pressure and the induction field, respectively, and σ_r and μ_r are the relative conductivity and permeability of the various materials.

3.3 Results from reference [14]

In reference [14], we have explored the range of the kinetic and magnetic Reynolds numbers and found dynamo action for $R_\mathrm{e}=1200$ and $R_\mathrm{m}\geq R_\mathrm{m}^c\approx 775$ when the solid walls of the vessel were assumed to be insulating. The growing magnetic field that is observed rotates in the precessing frame of reference and is dominated by the $m=2$ mode: as shown in Figure 9, the magnetic field lines show a mainly quadrupolar structure in the vacuum when seen from the top of the cylinder.

3.4 Numerical results with thick walls

We now present new results about thresholds and growing magnetic fields when using conducting walls of relative thickness $w=0.1$ at different places. The relative conductivity of these walls is chosen to be that of copper i.e., $\sigma_r=4.5$, and the relative magnetic permeability is $\mu_r=1$.

We investigate the MHD regime, where R_e and R_m are the two control parameters. As already observed for spherical and spheroidal dynamos, dynamo action occurs after symmetry breaking of the flow when the magnetic dissipation is small enough, i.e., for magnetic Reynolds numbers R_m above a critical value $R_\mathrm{m}^c(R_\mathrm{e})$. In order to study the influence of the conducting walls, we keep $R_\mathrm{e}=1200$ and vary R_m to find the threshold. We define four cases as follows. We call "insulating" case the configuration studied in reference [14], the "side" case corresponds to adding conducting walls on the cylindrical side of the vessel, the "lid" case corresponds to adding conducting walls at the top and bottom of the vessel, and the "wall" case corresponds to adding conducting walls everywhere. In all the cases the thickness of the wall is 0.1.

We first show in Figure 10a, a series of dynamo simulations done with $R_\mathrm{m}=300, 400$ and 900 for the "side" case. The figure shows the time evolution of the magnetic energy $M(t)=\int_{\Omega_c}\frac{1}{2}\mathbf{B}^2/\mu_0\mu_r d\tau$; dynamo action occurs when $M(t)$ is an increasing function of time. The initial magnetic fields at $R_\mathrm{m}=900$ is a small random seed but the initial velocity field is one obtained from the simulations described in Section 3.3. The initial velocity and magnetic fields for the run at $R_\mathrm{m}=400$ are the velocity and magnetic fields obtained from the run at $R_\mathrm{m}=900$ at time $t=47$. For $R_\mathrm{m}=300$, we restart from $R_\mathrm{m}=400$ at time $t=107$. Dynamo action occurs only for $R_\mathrm{m}=900$ and $R_\mathrm{m}=400$. Linear interpolation on the growth rates at $R_\mathrm{m}=300, 400$ and 900 gives the following estimate of the critical magnetic Reynolds number for the "side" case: $R_\mathrm{m}^c\approx 365$.

We have also performed series of simulations for the "lid" and "wall" cases by proceeding as above. The growth rates obtained from all these simulations are collected in Figure 10b. The estimated thresholds are $R_\mathrm{m}^c(\text{"side"})\approx 365\leq R_\mathrm{m}^c(\text{"wall"})\approx 650\leq R_\mathrm{m}^c(\text{"insulating"})\approx 775\leq R_\mathrm{m}^c(\text{'lid'})\approx 965$. We observe that adding "lids" is

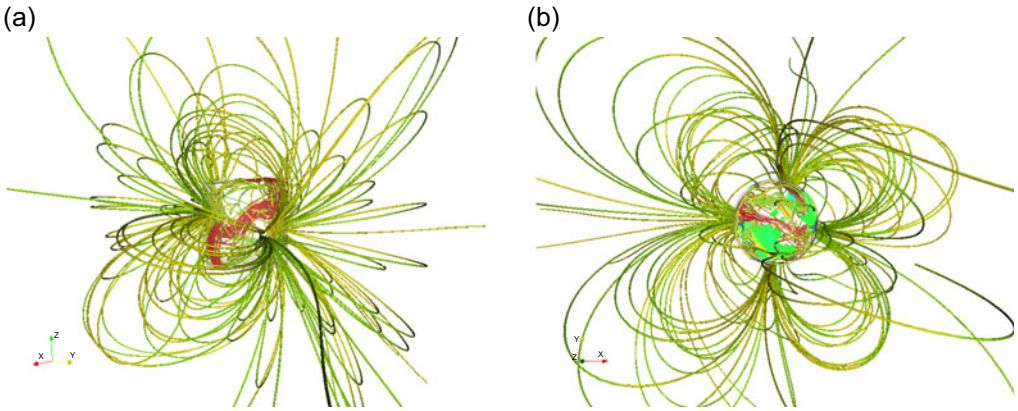

Fig. 9. Snapshot at $R_\mathrm{e}=1200$, $R_\mathrm{m}=2400$ for the "insulating" case showing vorticity field lines (red lines inside the cylinder) and magnetic field lines colored by the axial component (yellow [green] for positive [negative] h_z component): (a) perspective view, (b) from the top of the cylinder. From reference [14].

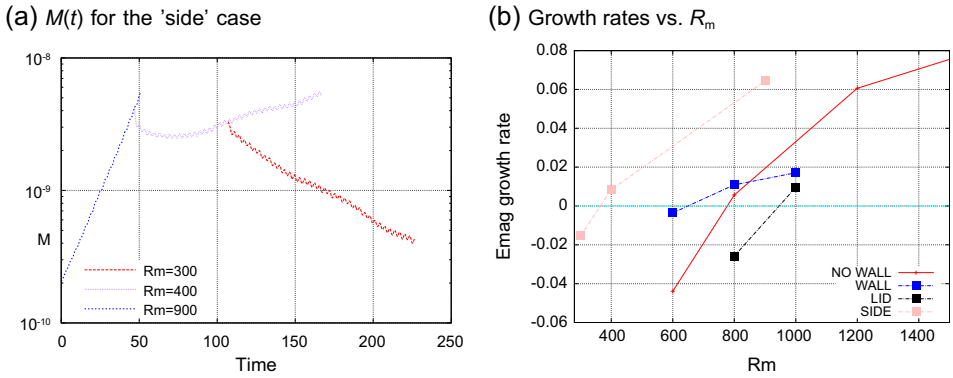

Fig. 10. (a) Time evolution of the magnetic energy $M(t)$ in the conducting fluid at $R_e = 1200$ and various R_m as indicated (in lin-log scale) for the "side" case; (b) growth rates of the magnetic field energy as a function of R_m for various configurations. The values are for $R_e = 1200$ and the thickness of either conducting wall type is taken as $0.1R$, with a relative conductivity $\sigma_r = 4.5$.

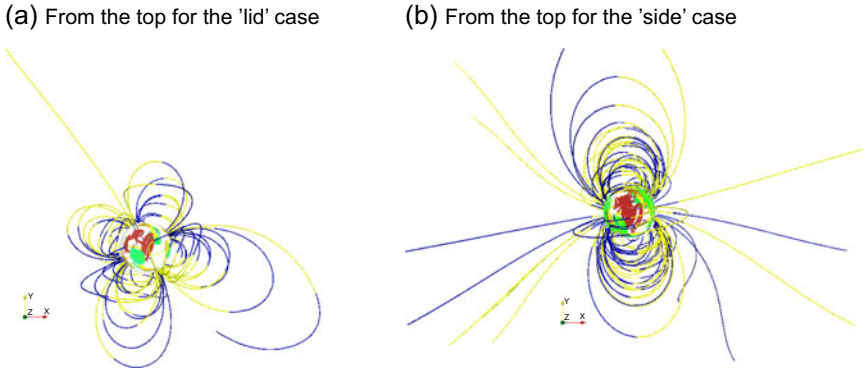

Fig. 11. Snapshots at (a) $R_e = 1200$, $R_m = 1000$ for the "lid" case and (b) $R_e = 1200$, $R_m = 900$ for the "side" case showing vorticity field lines (red lines inside the cylinder) and magnetic field lines colored by the axial component (yellow [blue] for positive [negative] h_z component).

detrimental to the dynamo action while adding "side" walls helps it. These results are reminiscent of those found by [19,28].

Conducting walls enable currents to loop on longer scales but also lead to different growing magnetic field structures as shown in Figure 11. Both the "lid" and the "insulating" configurations give a magnetic field that is mainly quadrupolar while the "side" configuration generates a growing magnetic field that is mainly dipolar and equatorial. We have also done computations with ferromagnetic walls (to be reported elsewhere), and we have observed that the critical magnetic Reynolds number increases with respect to μ_r in the three cases ("lid", "side", "wall"). Further investigations about the distribution of the current density and of the dissipation are planned in the next future.

Although a predictive explanation of the variation of the dynamo threshold is still lacking at the present time, the impact of the nature of the walls seems crucial for the design of experimental precession-driven fluid dynamos. The increase of R_m^c from the "side" case to the "lid" case suggests to diminish the influence of the lid by lowering its conductivity.

4 Conclusion

We are currently developing algorithms aiming at realistically reproducing the VKS dynamo. One important challenge is to properly implement jump conditions on moving boundaries to account for blades made of soft iron in the magnetic induction solver. Another challenge is to model the non-axisymmetric blades in the Navier-Stokes solver. We are currently developing a penalty method for this purpose, see Figure 7.

Our results on the precessing cylinder are encouraging for the optimization of the critical magnetic Reynolds number for the planned experiment at DRESDYN [5], where magnetic Reynolds number as large as 700 are expected to be reached. The question of self-excitation in a real precession experiment is far from being settled though.

The HPC resources for SFEMaNS were provided by GENCI-IDRIS (Grant 2014-0254) in France. J.-L. Guermond acknowledges support from University Paris Sud 11 and the National Science Foundation Grant NSF DMS-1015984.

References

1. A. Gailitis, O. Lielausis, S. Dement'ev, E. Platacis, A. Cifersons, Phys. Rev. Lett. **84**, 4365 (2000)
2. R. Stieglitz, U. Müller, Phys. Fluids **13**, 561 (2001)
3. R. Monchaux, M. Berhanu, M. Bourgoin, Ph. Odier, M. Moulin, J.-F. Pinton, R. Volk, S. Fauve, N. Mordant, F. Pétrélis, A. Chiffaudel, F. Daviaud, B. Dubrulle, C. Gasquet, L. Marié, F. Ravelet, Phys. Rev. Lett. **98**, 044502 (2007)
4. S. Miralles, N. Bonnefoy, M. Bourgoin, Ph. Odier, J.-F. Pinton, N. Plihon, G. Verhille, J. Boisson, F. Daviaud, B. Dubrulle, Phys. Rev. E **88**, 013002 (2013)
5. F. Stefani, S. Eckert, G. Gerbeth, A. Giesecke, Th. Gundrum, C. Steglich, T. Weier, B. Wustmann, Magnetohydrodynamics **48**, 103 (2012)
6. W.V.R. Malkus, Science **160**, 259 (1968)
7. J.-L. Guermond, R. Laguerre, J. Léorat, C. Nore, J. Comput. Phys. **221**, 349 (2007)
8. J.-L. Guermond, R. Laguerre, J. Léorat, C. Nore, J. Comput. Phys. **228**, 2739 (2009)
9. J.-L. Guermond, J. Léorat, F. Luddens, C. Nore, A. Ribeiro, J. Comput. Phys. **230**, 6299 (2011)
10. A. Giesecke, C. Nore, F. Plunian, R. Laguerre, A. Ribeiro, F. Stefani, G. Gerbeth, J. Léorat, J.-L. Guermond, Geophys. Astrophys. Fluid Dyn. **104**, 249 (2010)
11. A. Giesecke, C. Nore, F. Stefani, G. Gerbeth, J. Léorat, F. Luddens, J.-L. Guermond, Geophys. Astrophys. Fluid Dyn. **104**, 505 (2010)
12. A. Giesecke, C. Nore, F. Stefani, G. Gerbeth, J. Léorat, W. Herreman, F. Luddens, J.-L. Guermond, New J. Phys. **14**, 053005 (2012)
13. C. Nore, J. Léorat, J.-L. Guermond, A. Giesecke, Phys. Rev. E **91**, 013008 (2015)
14. C. Nore, J. Léorat, J.-L. Guermond, F. Luddens, Phys. Rev. E **84**, 016317 (2011)
15. F. Ravelet, A. Chiffaudel, F. Daviaud, J. Léorat, Phys. Fluids **17**, 117104 (2005)
16. L. Marié, C. Normand, F. Daviaud, Phys. Fluids **18**, 017102 (2006)
17. G. Verhille, N. Plihon, M. Bourgoin, Ph. Odier, J.-F. Pinton, New J. Phys. **12**, 033006 (2010)
18. T.G. Cowling, Mon. Not. R. Astron. Soc. **94**, 39 (1934)
19. F. Stefani, M. Xu, G. Gerbeth, F. Ravelet, A. Chiffaudel, F. Daviaud, J. Léorat, Eur. J. Mech. B: Fluids **25**, 894 (2006)
20. F. Krause, K.-H. Radler, *Mean-Field Magnetohydrodynamics, Dynamo Theory* (Pergamon Press Oxford, New York, NY, 1980)
21. R. Laguerre, C. Nore, A. Ribeiro, J. Léorat, J.-L. Guermond, F. Plunian, Phys. Rev. Lett. **101**, 104501 (2008)
22. F. Ravelet, B. Dubrulle, F. Daviaud, P.-A. Ratié, Phys. Rev. Lett. **109**, 024503 (2012)
23. J. Boisson, S. Aumaitre, N. Bonnefoy, M. Bourgoin, F. Daviaud, B. Dubrulle, Ph. Odier, J.-F. Pinton, N. Plihon, G. Verhille, New J. Phys. **14**, 013044 (2012)
24. H. Zaidi, C. Nore, A. Bossavit, F. Bouillault, J.-L. Guermond, Whitney Element Approach For Dynamo Action Modeling With a Von Kármán Type Velocity, in *IEEE Transaction on Magnetics, Sixth biennal IEEE Conference on Electromagentic Filed Computation, Annecy, France, 2014* (Poster PA3:9)
25. S. Kreuzahler, D. Schulz, H. Homann, Y. Ponty, R. Grauer, New J. Phys. **16**, 103001 (2014)
26. A. Tilgner, Phys. Fluids **17**, 034104 (2005)
27. C.-C. Wu, P. Roberts, Geophys. Astrophys. Fluid Dyn. **103**, 467 (2009)
28. R. Laguerre, C. Nore, J. Léorat, J.-L. Guermond, CR Mécanique **334**, 593 (2006)